

Effect of Graphene Interface on Potassiation in a Graphene- Selenium Heterostructure Cathode for Potassium-ion Batteries

Vidushi Sharma and Dibakar Datta**

Department of Mechanical and Industrial Engineering, New Jersey Institute of Technology,
Newark, New Jersey 07103, United States

*Corresponding Authors

Vidushi Sharma, Email: vs574@njit.edu, vidushis@ibm.com

Dibakar Datta, Email: dibakar.datta@njit.edu

KEYWORDS: Selenium Cathode, Heterostructure Electrodes, Potassium-ion Battery, Graphene, Density Functional Theory, Interface

ABSTRACT

Selenium (Se) cathodes are an exciting emerging high energy density storage system for Potassium ion batteries (KIB), where potassiation reactions are less understood. Here, we present an atomic-level investigation of $K_x\text{Se}$ cathode enclosed in hexagonal lattices of carbon(C) characteristic of multilayered graphene matrix and multiwalled carbon nanotubes (MW-CNTs). Microstructural changes directed by graphene substrate in $K_x\text{Se}$ cathode are contrasted with graphene-free cathode. Graphene's binding affinity for long-chain polyselenides ($\text{Se}_3 = -2.82$ eV and $\text{Se}_2 = -2.646$ eV) and

ability to induce reactivity between Se and K are investigated. Furthermore, intercalation voltage for graphene enclosed $K_x\text{Se}$ cathode reaction intermediates are calculated with $K_2\text{Se}$ as the final discharged product. Our results indicate a single-step reaction near a voltage of 1.55 V between K and Se cathode. Our findings suggest that operating at higher voltages ($\sim 2\text{V}$) could result in the formation of reaction intermediates where intercalation/deintercalation of K could be a challenge, and therefore cause irreversible capacity losses in the battery. Primary issues are the high binding energy of long-chain polyselenides with graphene that discourage K storage and Se-Se bond dissociation at low K concentrations. A comparison with graphene-free cathode highlights the substantial changes a van der Waals (vdW) graphene interface can bring in atomic-structure and electrochemistry of the $K_x\text{Se}$ cathode.

Keywords: Selenium Cathode, Heterostructure Electrodes, Potassium-ion battery, Graphene, Density Functional Theory, Interface

1. Introduction

Current innovations in energy sector are focused on balancing the world energy consumption with clean energy solutions. Massive research and development efforts are made in the past few decades to advance lithium-ion battery (LIB) stature to the primary energy storage for most engineering applications, including electronic devices, transportation, wearables, etc.[1, 2] The rarity of Li and cost associated with development of LIBs strongly advise the use of low cost complements such as sodium-ion batteries (NIBs) and potassium-ion batteries (KIBs) in applications where maximizing energy and power is not essential such as in small-scale energy applications.[3] Particularly, KIBs have garnered interest as low cost complements of LIBs owing to the relative earthly abundant battery precursor materials. [4-7] Energy storage mechanism in KIB is similar to

'rocking chair' operation in LIBs, except for the respectively larger ion carriers that greatly differentiate the electrode intercalation mechanism and diffusion kinetics in KIB battery systems. This suggests careful tailoring of the structural design of electrodes[3] for next generation sustainable KIB batteries.

Among low cost alternatives to Li for energy storage, K has a lower standard reduction potential, which is closer to Li ($-3.04\text{V } E^0 = \text{Li}^+/\text{Li}^- < -2.93\text{V } E^0 = \text{K}^+/\text{K}^- < -2.71\text{V } E^0 = \text{Na}^+/\text{Na}^-$).[3] This permits KIBs to operate at higher potentials with better energy density than NIBs.[8] Moreover, the ionic mobility of K remains unhindered by its weight and is competitive to Li.[9] On the electrode front, the commercial graphite anode used in LIB can be customized easily for KIB. K intercalated graphite is found stable even at a high alkali density of KC_8 . [10] The electrochemical analysis by Komaba et al. demonstrated graphite anode to have 244 mAhg^{-1} reversible capacity for KIB in 0 - 0.3 V range.[9] Likewise, most commercially acceptable LIB anodes perform well for KIBs at relatively safer voltages.[8] However, KIB cathodes become rather challenging to design due to the large size of K ion. Transition metal layered oxide cathodes exhibit fast capacity fading in KIB because it is not easy to extract or re-intercalate large K ions without any structural damage.[11] Layered birnessite $\text{K}_{0.3}\text{MnO}_2$ was one of the first layered oxide cathodes investigated for KIB by Vaalma et al.[12] in non-aqueous electrolyte, that only showed a reversible capacity of 65 mAhg^{-1} between 3.5 - 1.5V and 57% capacity retention. Instead, metal organic frameworks (MOFs) are preferred alternatives to layered oxides as KIB cathodes. Pore sizes on MOF are adjustable and promising for reversible K storage. Eftekhari et al. introduced K containing MOF called Prussian Blue (PB) cathode $\text{KFe}_4^{\text{III}}[\text{Fe}^{\text{II}}(\text{CN})_6]$, which could achieve 78.62 mAhg^{-1} reversible capacity and only 12% capacity fade post 500 cycles.[6] This stability marked PB as a prospective cathode for KIB and encouraged experimental electrochemical studies on

several PB analogs.[13-16] Despite all efforts, high energy density cathodes still remain a major limiting factor in development and adoption of KIB.

Chalcogenides like sulfur (S) and selenium (Se) store metal ions by conversion reactions that benefit energy densities. [17-22] However, these promising electrodes suffer from poor reversibility due to dissolution of reaction intermediates in the electrolyte and pulverization caused by large volume expansions.[17-22] Se is comparatively heavier, less reactive, and more electroconductive than S,[23, 24] which imply Se-based cathodes can have good electron transport and better control over shuttle effects if well engineered with confining composite matrix. Liu et al. were the first to report performance of Se cathode confined in carbonized polyacrylonitrile for KIB in 2017.[25] Active Se in composite maintained a reversible capacity of 396 mAhg⁻¹ with K₂Se as a final discharged product. One added problem identified for K-Se batteries is limited reactivity of both metals due to their large atomic size.[26] The strategy of confining Se in carbon (C) allotropes to control surface reactivity, phase transition, and volume change in Se cathode has been well explored for LIBs and next-generation metal batteries.[20, 21, 27-36] However, the role of Se supporting C matrix goes beyond polyselenide confinement to providing an interface for easy expansion and contraction of Se during battery cycles. [37, 38] Interestingly, refined hexagonal C lattice such as graphene(Gr) have the advantage of a slippery van der Waals surface that is shown to be effective in combating stresses in alloying electrodes upon ion storage, thereby improving the cycle life of the composite electrode.[37] We previously reported the detailed characterization of the Se-Gr interface and its promising potential in mitigating interfacial stresses due to low interface adhesion (0.43 J/m²)[38] which was comparable to the silicon (Si) – Gr system reported by Basu et al.[37] There is also supportive evidence in literature about enhanced

electrochemical activity of Se cathode when encapsulated in hexagonal C lattice such as graphene and carbon nanotubes (CNT).[27, 39] [40-43]

In present work, we further explore the effects of interface presented by graphene to Se cathode in a 3D-2D heterostructure electrode for application in next-generation KIB battery by computational methods. Latest simulation results have confirmed that hexagonal lattice of C has a strong chemical affinity for K_2Se . [27] Therefore, we use K_2Se as the final discharged product of Se and compare the electrochemical voltage profile of graphene-free Se cathode with graphene-supported Se cathode. K intercalation and distribution is modeled in reaction intermediates between Se cathode and discharged product K_2Se for graphene free along as well as graphene-supported configurations. Microstructural changes at graphene- K_xSe interface are investigated and further decomposed into Se-K clusters whose binding energy with graphene substrate is calculated. We calculate the operational voltage to direct single-step K_2Se cathode discharging in a graphene enclosure. Substantial electrochemical changes that a graphene interface brings in the cathode without covalent bonding with Se-K have been highlighted.

2. Methodology

2.1. Structure of Graphene supported Se cathode.

Amorphous Se (a-Se) was derived by computational quenching of monoclinic selenium-containing Se_8 rings that break to form different sized polymeric chains with Se-Se bond length of 2.4 Å. The complete computational modeling and characterization of a-Se and a-Se/Gr have been reported in our previous study.[38] The exact chemical steps preparing Se-C heterostructure electrodes can deviate based on targeted nanostructures and C matrix.[3, 44, 45] Se infusion process in graphene-based matrix typically involves high temperature conditions followed by condensation.[46, 47] This results in evenly distributed Se on the substrate surface.[21] In battery set-ups, Se is mostly

in amorphous form with Se_n chains ($n = 2$ to 8).[36] Alternatively, if originally used in crystalline form, Se_8 rings are converted to Se_n chains after the first battery cycle and remain so for the rest of the battery life.[48] Structural parameters such as interatomic bond lengths, bond angles, and dihedral angles are comparable among pristine Se allotropes,[49, 50] yet graphene matrix surface can direct the aligned distribution of Se. Therefore, we modeled our a-Se/Gr cathode keeping experimentally synthesized structures in mind.[46]

To generate 3D periodic configurations of a- K_xSe cathode supported over graphene substrate, we started with an optimized amorphous a- Se_{30} system (Figure 1(a)) and sequentially added 6 K atoms at a time until a- $\text{K}_{60}\text{Se}_{30}$ (a- K_2Se) is achieved (Figure 1(b)). After each potassium addition step, K atoms were allowed to diffuse in the cathode during an ab initio molecular dynamics simulation (AIMD) run and then relaxed with density functional theory (DFT) until energy-optimized a- K_xSe structures were obtained. Volume of the simulation cell was allowed to ease in all dimensions. Between initial Se and final a- $\text{K}_{60}\text{Se}_{30}$ (Figure 1(a-b)), 183.52% volume expansion was noted. The simulation cell's base also expanded during potassiation, and its x-y dimensions were used to determine graphene substrate's size. The final a- $\text{K}_{60}\text{Se}_{30}$ bulk configuration was placed on top of a periodic graphene lattice containing 96 sp^2 hybridized carbon atoms with the interfacial gap of ~ 2.8 Å to form the a- $\text{K}_{60}\text{Se}_{30}/\text{Gr}$ interface (a- $\text{K}_2\text{Se}/\text{Gr}$). Note that the surface area of graphene substrate was equivalent to the x - y surface of final a- $\text{K}_{60}\text{Se}_{30}$. We further let the atoms diffuse and re-adjust on the graphene lattice during an AIMD run followed by DFT optimization. For graphene-supported K-Se cathode, optimized a- $\text{K}_2\text{Se}/\text{Gr}$ configuration was considered the final discharged product (Figure 1(c)). Starting from this a- $\text{K}_2\text{Se}/\text{Gr}$ structure, 6 K atoms were sequentially removed, followed by AIMD run and complete energy optimization, until a- Se_{30}/Gr is left (Figure 1(d)). Upon complete charging (depotassiation), the end structure

resembles a-Se clusters distributed on a periodic graphene mesh (Figure 2(a)). This computationally modeled configuration is close to experimentally synthesized nano architectures of active electrodes and graphene.[46, 51-53] Interlayer spacing between the graphene sheets in charged(depotassiated, Figure 2(a)) and discharged (potassiated, Figure 2(b)) a-Se/Gr cathode are 9 Å and 18.57 Å, respectively. These microporous confinement orders of Se between graphene sheets are also similar to the earlier Se confinement report.[54]

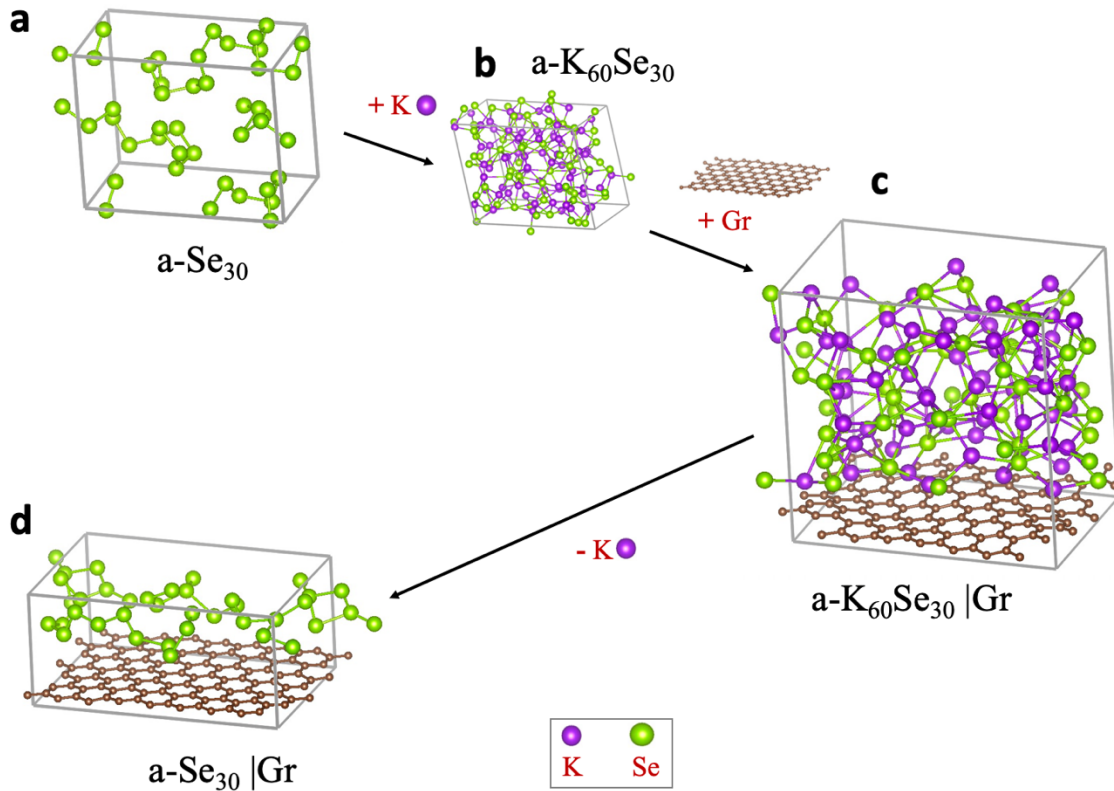


Figure 1. (a) Atomic representation of initial optimized amorphous Se (a-Se₃₀) generated from a crystalline Se with computational quenching. The structure is dominated by disintegrated forms of Se rings as chains with nearest neighboring distance of ~2.4Å. (b) Miniaturized view of a-K₆₀Se₃₀ (a-K₂Se) generated after complete potassiation (discharging). The volume is expanded by 183.52

%. **(c)** Atomic representation of $a\text{-K}_{60}\text{Se}_{30} / \text{Gr}$ ($a\text{-K}_2\text{Se}/\text{Gr}$) system. Graphene with surface area equivalent to the base of $a\text{-K}_{60}\text{Se}_{30}$ was added in z dimension. **(d)** Completely charged $a\text{-Se}_{30}/\text{Gr}$ cathode post potassium removal. The structure once again forms Se chains that are slightly condensed towards graphene surface.

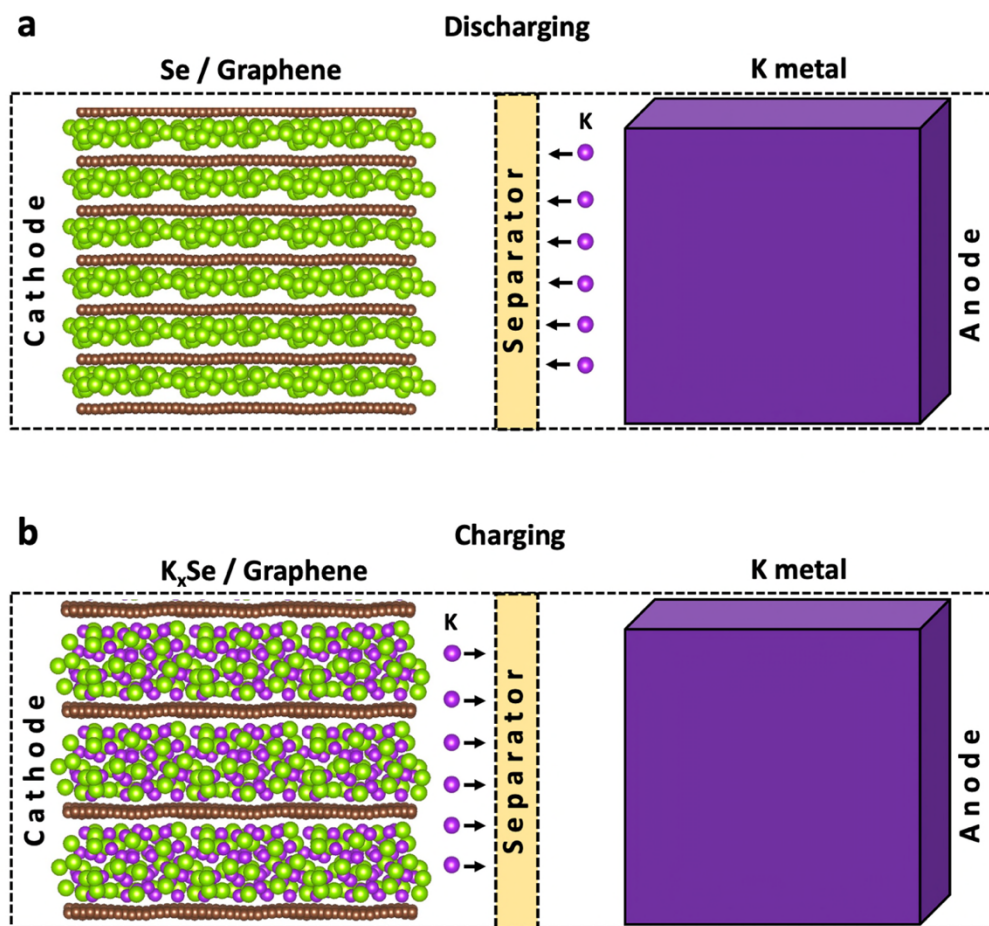


Figure 2. Schematic representation of a selenium-graphene heterostructure cathode half-cell during **(a)** discharging and **(b)** charging process. Interlayer spaces between two graphene sheets represent pores for Se in graphene-based matrix and is approximately 9\AA (depotassiated) and 18\AA (potassiated).

2.2. Computational Details

All AIMD and DFT simulations were performed in Vienna Ab initio Simulation Package (VASP).[55] Inert core electrons were mimicked by Projector-augmented-wave (PAW) potentials and valence electrons were represented by plane-wave basis set with energy cut off at 550eV.[56, 57] The GGA-PBE exchange-correlation function was taken into account for all calculations.[58] AIMD simulations were run with 1 fs time interval, temperature set at 300 K within NVT ensemble, and 2 X 2 X 2 gamma centered k-meshes. For all DFT calculations, the conjugate gradient method was employed for energy minimization with Hellmann-Feynman forces less than 0.02 eV/Å and convergence tolerance set to 1.0×10^{-4} eV. Gamma-centered 4 X 4 X 4 k-meshes were taken for good accuracy. Only for graphene-supported cathodes, GGA functional was inclusive of vdW correction to incorporate the effect of weak long-range van der Waals (vdW) forces. [59] All calculations for graphene-supported cathode were done with optPBE functional within vdW-DF-family. [60, 61]

3. Results and discussion

3.1. Potassium segregation at the interface.

The presence of graphene substrate is reportedly beneficial for the Se electrode to control the dissolution of polyselenides in electrolytes and provide a supportive matrix to the volume fluctuating electrode.[46, 52, 53] However, graphene and pristine a-Se do not form a very reliable interface from a physicochemical perspective.[38] On a positive note, low interface strength (0.34 J/m²) between Se and graphene indicates Se electrode interfaced with graphene can easily expand/contract during the battery cycle and evade high mechanical stresses.[37, 38] On the downside, the two materials are held by weak van der Waals (vdW) forces and have a very high

potential gradient at the interface.[38] This condition is subjected to change as K atoms enter Se bulk due to prospective phase changes and different binding affinities of both atom types with graphene. Therefore, we expect distinct microstructural order in graphene supported $a\text{-K}_x\text{Se}$ cathode from its free counterpart. Figure 3 presents relaxed atomic structures of $a\text{-K}_x\text{Se}$ cathodes with and without graphene substrate, together with the respective variations of atomic K/Se ratio along the z-dimension.

To determine the influence of graphene substrate on the distribution of K and Se atoms, the atomic K/Se ratio profile is traced in three high K cathode configurations: $a\text{-K}_2\text{Se}$, $a\text{-K}_{1.6}\text{Se}$, and $a\text{-KSe}$. Figure 3(a) demonstrates the K/Se ratio profiles in cathode configurations with graphene support while their graphene-free counterparts are analyzed in Figure 3(b). Simulation cells are divided into four bins (bin ID = 1, 2, 3, 4) along z-direction. In graphene-supported structures, the bottom 3.4 Å is not included in the bins considering it to be the vdW radius of graphene and represents volume occupied by only graphene. The rest of the simulation cell ($z - 3.4$ Å) is divided into bins of width ranging from 3.18 Å to 3.8 Å depending upon the $a\text{-K}_x\text{Se}$ thickness. For graphene-free $a\text{-K}_x\text{Se}$, bin widths ranged between 3.6 Å to 4 Å. The atomic K/Se ratios in each bin are marked with red and connected by blue line to view the pattern. The average K/Se ratio in the entire bulk (x in $a\text{-K}_x\text{Se}$) is plotted as the dashed yellow line for comparison purposes.

In graphene-supported $a\text{-K}_x\text{Se}$ (Figure 3(a)), two prominent regions can be noted based on K/Se ratio analysis: K-rich and K-deficient. K/Se ratios in bins 1 and 4 (close to graphene surface) clearly demonstrate higher K concentration (Figure 3(a)). In contrast, bin 2 (further from the graphene surface) has a low K concentration in all three cathode configurations (Figure 3(a)), i.e., K/Se = 2, 1.6, and 1. Combined K/Se ratio in bins 1 and 4 is continually above-average (yellow line) bulk K/Se ratio. A clear K concentration gradient is observed in sub-interfacial region (bin

ID 1,4) and central region (bin ID 2,3). These plots indicate affinity of K atom to graphene surface and the possibility of K segregation at the interface. The balance of K concentration in electrode could be decided by observing bin-wise K/Se ratios (red) with respect to the average value (yellow line). The K concentration in completely discharged cathode a-K₂Se/Gr appears to be balanced. As shown in Figure 3(a1), bins 1 and 3 have average K/Se concentration value (*i.e.*, $x = 2$) that falls on the yellow line. However, K/Se concentration value in bins 2 and 4 is less and more than the average ($x=2$), respectively. In contrast, for a-K_{1.6}Se/Gr and a-KSe/Gr shown in Figure 3(a2-a3), K concentrations are higher than the average ($x=1.6$ and $x=1$, respectively) in three out of four bins (bin 1,3,4) suggesting a misbalance of K distribution in intermediate cathode structures.

The plots in Figure 3(b) represent K/Se ratios in graphene-free a-K_xSe cathode configurations and demonstrate alternative fluctuations of K/Se ratios within bins. It is important to remember that in these atomic representations of cathode without graphene, a-K_xSe cathodes are continuous periodic bulks. Understandably, a bin with high K concentration is followed by bin with low K concentration. No distinct pattern of K distribution can be recognized without a substrate. Moreover, K/Se ratio plot for low K concentration ($K/Se \leq 1$) cathode in Figure 3(b3) is similar to graphene supported one (Figure 3(a3)), indicating that at low K content, segregation effect of graphene is reduced. Furthermore, all a-K_xSe structures in our study remained amorphous for both graphene-supported and graphene-free cases, as discussed in next section. However, it is unclear whether the segregation of K atoms at the graphene interface causes the formation of any new phase or phase boundary. The system size considered in our atomic study is too small to determine any phase transitions and phase boundaries. Nevertheless, the presence of graphene substrate creates a significant chemical gradient inside K-Se cathode intermediates (Figure 3(a))

and an imbalance in K concentration, which affects the site-specific energy of K atoms in the cathode[62] and stability of structural intermediates.

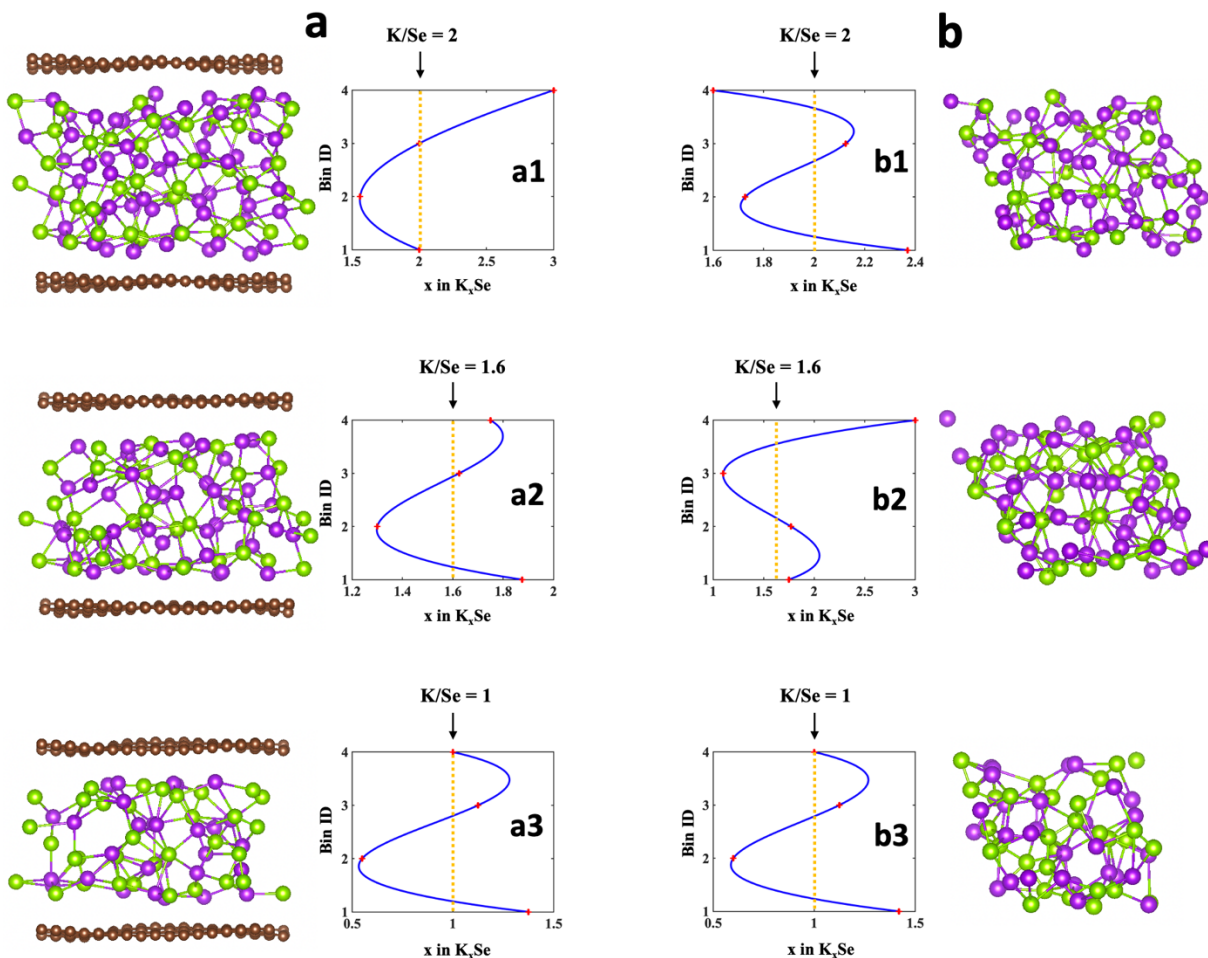


Figure 3. Degree of K segregation and K/Se ratio profile for **(a)** periodic $a\text{-K}_x\text{Se}/\text{Gr}$ and **(b)** periodic $a\text{-K}_x\text{Se}$ without any graphene support. Structures are divided into four bins along z dimension noted as Bin ID 1- 4. K/Se ratios in each bin are marked with red and connected by blue line to preview the pattern. Average K/Se ratio in the entire bulk is plotted as dashed yellow line for comparison purpose. Graphene supported cathodes with over-all high average K ratio (>1) demonstrate higher K concentrations closer to graphene surface (Bin ID 1 and 3). In periodic $a\text{-}$

K_x Se cathodes without graphene substrate, K concentration peaked alternatively in bins. In cathodes with lower average K/Se ratio (≤ 1), distribution of K is nearly same irrespective of graphene presence.

3.2. Microstructural analysis.

Pristine graphene does not form any strong covalent bonds with active cathode due to its vdW slippery surface. Despite the non-reactive surface, graphene presence causes K concentration gradient in the active K_x Se cathode as noted in the previous section. This opens possibilities of variations in bond lengths and cluster formations at the interface. We determined nearest neighboring distances between the atom pairs (Se-Se, Se-K, and K-K) in a- K_x Se cathodes by radial distribution function (RDF) analysis represented in Figure 4. RDF provides short-range and long-range structural information about the system as the function of distances between the atomic pairs. Crystallinity is recognized by sharp singular distinct peaks in the plots, while broad peaks are characteristic of amorphous structure. RDF plots of completely discharged and partly discharged a- K_x Se ($x= 2$ and 1) configurations in the graphene-supported systems (Figures 4(c-d)) are compared with graphene-free cases (Figure 4(a-b)). The important peaks for neighboring distances between Se-Se, Se-K, K-K atomic pairs are listed in Table 1. Crystalline c- K_2 Se and c-KSe systems are obtained from Materials Project database and their RDF analysis is used as a comparative standard to identify any signs of short-range crystalline order in amorphous atomic systems in our study.[63] In c- K_2 Se (Figure 5(a)), nearest neighboring distance of 5.5Å for Se-Se atom pair denotes that no Se-Se covalent bonds are present in the structure. Similarly, no K-K bond pairs are present in the same structure. All Se atoms are bonded with K atoms with the bond length of 3.35Å in the crystal configuration shown in Figure 5(a). In contrast, we observe more Se-Se bond pairs

with bond length of 2.5\AA in the atomic configuration of c-KSe with low K content (as shown in Figure 5(b)).

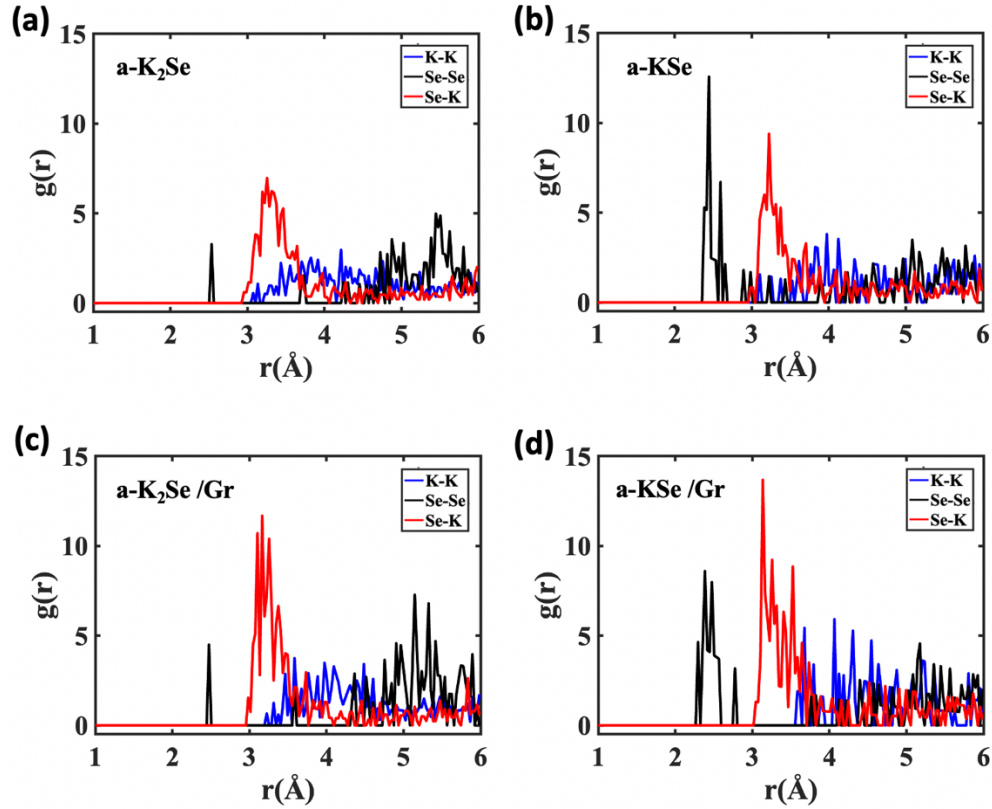


Figure 4 Radial distribution function (RDF) plots exhibiting nearest neighboring distances between atomic pairs in graphene free configurations (a) a-K₂Se, (b) a-KSe, and graphene supported configurations (c) a-K₂Se/Gr, (d) a-KSe/Gr. Distances between atomic pairs are plotted as Se-Se with black, Se-K with red and K-K with blue.

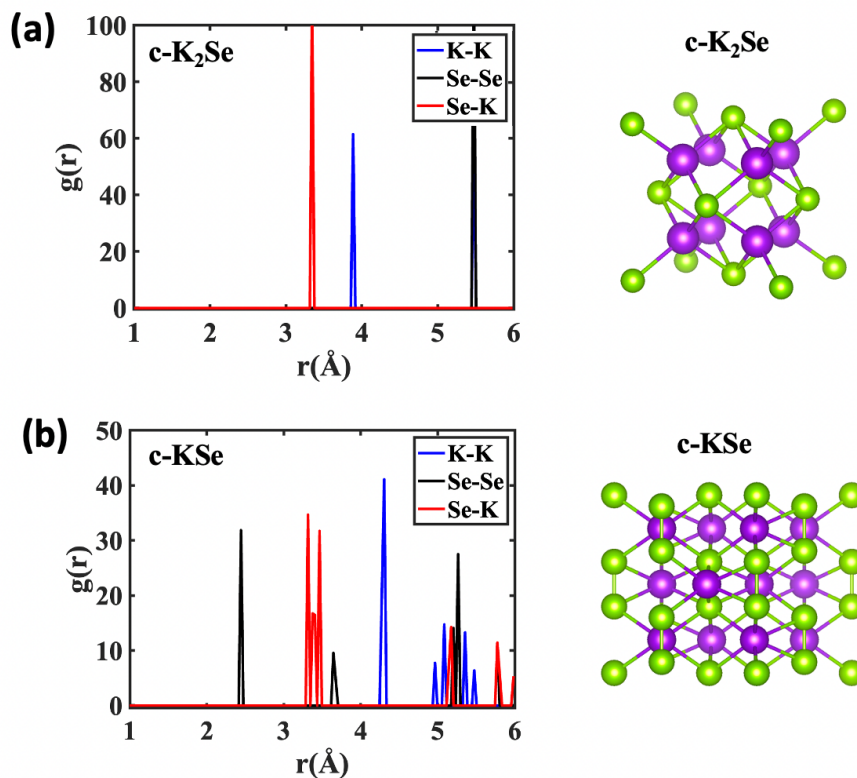


Figure 5 Radial distribution function (RDF) plots exhibiting nearest neighboring distances between atomic pairs in **(a)** $c\text{-K}_2\text{Se}$ derived from Materials Project Database mp-8426 and **(b)** $c\text{-KSe}$ derived from Materials Project Database mp-9268. Distances between atomic pairs are plotted as Se-Se with black, Se-K with red and K-K with blue.

In graphene-free cathodes, the existence of long-range amorphous characteristics can be concluded from the RDF analysis. Peaks at 2.5 Å are noted in the RDF of $a\text{-K}_x\text{Se}$ systems, which indicate the presence of a few Se-Se covalent bonds. This peak is smaller and narrower in high K concentration cathode ($a\text{-K}_2\text{Se}$), while it is intense and broader in low K concentration cathode ($a\text{-KSe}$). As the concentration of K is twice the Se in $a\text{-K}_2\text{Se}$, Se-K bonds are prominent observations in Figure 4(a) with bond lengths of $\sim 3.25\text{Å}$ and 3.35Å . The red peaks at 2.9-3.4 Å are representative of Se-K distances and have a broad base. These peaks strongly contrast with very defined plots in

crystalline configurations in Figure 5. In both a-K_xSe systems, K forms strong covalent bonds with Se. Hence, no prominent K-K bond pairs are noticed in the RDF analysis. The K-K values in Table 1 represent the neighboring distances and not bond lengths.

In graphene-supported cathodes, red peaks that are representative of Se-K bond become highly intense. Increase in Se-K bond pairs along with evidence of K segregation at the interface in previous section, imply that graphene induces reactivity between Se and K in the system. There is also cue from previous studies[38] that the presence of graphene reduces mobility gap in a-Se, thereby making the electronic states more continuous and system more conductive. In reciprocal, the electronegative Se also manipulates the surface chemistry of graphene substrate and activates it to provide additional K storage sites.[23, 64-66] Though it remains unclear if the presence of graphene substrate induces any short-range crystallinity in the cathodes or not, graphene undoubtedly causes Se chain dissociations and enhanced K reactivity at the interface.

Table 1. Nearest neighboring distances (Å) between Se-Se, Se-K and K-K in the K_xSe cathodes with and without graphene substrate

System	Se-Se	Se-K	K-K	Characteristic
a-K ₂ Se	2.5 Å, 4.9 Å, 5.5 Å	3.25 Å	>3 Å	Amorphous
a-K ₂ Se/Gr	2.4 Å, 4.4 Å, 5.2 Å	3.2 Å	>3.2Å	Amorphous
c-K ₂ Se	5.5 Å	3.35 Å	3.8 Å	Crystalline
a-KSe	2.5Å	3.2Å	>3.0Å	Amorphous
a-KSe/Gr	2.5 Å, 2.8 Å	3.2Å	>3.5Å	Amorphous
c-KSe	2.5Å, 3.7Å, 5.2Å	3.3Å, 3.5Å	4.3Å, 4.9Å, 5.4Å	Crystalline

Note: 'a-' denotes amorphous structure and 'c-' denote crystalline structures

One standalone difference between high K cathode (a-K₂Se) and low K cathode (a-KSe) configurations in Figure 4 is the peak intensity at 2.5Å for Se-Se bonds. As earlier mentioned, a small peak at 2.5Å in a-K₂Se (both graphene-free and graphene-supported cathodes) indicates the presence of only a few Se-Se covalent bonds. This peak becomes very prominent in a-KSe (both graphene-free and graphene-supported cathodes), signifying Se-Se bonds are more profound. Se retains their chained structures at low K concentrations. This causes key differences in the Se-K microstructures that are observed in low K (a-KSe/Gr) and high K (a-K₂Se/Gr) cathodes interfaced with graphene. In the former, the majority Se-Se bonds are intact, and interface contains potassium polyselenides with two to three Se atoms at the center surrounded by K atoms. When K concentration is further lowered ($x < 1$ in K_xSe), Se chains become longer. Meanwhile, as K concentration increases, most Se-Se bonds break to accommodate K. The resulting interface contains Se-K clusters with one Se atom at the center bound by multiple K atoms. Inspired by these inferences, we analyzed the Se-K clusters at graphene interface in a-KSe/Gr and a-K₂Se/Gr to determine their adsorption energy E_{ad} over the graphene surface. Polyselenides in a-KSe/Gr (Figure 6(a)) are labeled as cluster-1 (Se-Se) and cluster-2 (Se-Se-Se). As discussed earlier, a-KSe/Gr was created after sequential depotassiation from a-K₂Se/Gr. Hence, Se-Se bonds in a-KSe/Gr are formed after K was removed (charging) and are not present due to the initial a-Se₃₀ chain structure. Meanwhile, a K saturation in a-K₂Se/Gr causes each Se atom to be surrounded by many K atoms (4 to 7). Typically, three Se-K clusters were present at the interface: Se₁K₅ labeled as cluster-3, Se₁K₆ labeled as cluster-4, and Se₁K₇ labeled as cluster-5 (Figure 6(b)). Only the Se atoms present near the graphene surface (bin ID 1) were bound to 6 or 7 K atoms, while Se in the central region (bin ID 2 and 3) were bound to 4 or 5 K atoms.

The surface adsorbed clusters were isolated from the bulk, and their adsorption energies (E_{ad}) over graphene substrate were determined as follows

$$E_{ad} = E_{total} - E_{cluster} - E_{graphene} \quad (1)$$

Where E_{total} is the energy of cluster over graphene substrate determined by DFT, $E_{cluster}$ and $E_{graphene}$ are the energy of the isolated cluster and pristine graphene substrate. Negative E_{ad} denotes thermodynamically favored adsorption. We do not consider distinct translational or rotational configurations of Se-K clusters and limit our analysis to their existent orientation found in the parent bulk models (a-KSe/Gr and a-K₂Se/Gr). Stability of isolated clusters is realized from $E_{cluster}$ values (Figure 6(c)) in the order cluster-2 > cluster-1 > cluster-3 > cluster-4 > cluster-5. Polyselenides (cluster-1 and 2) are naturally more stable than high-K clusters (cluster 4 and 5). Our thermodynamic values indicate that high-K clusters cannot exist independently outside the graphene-supported cathode bulk. Therefore, high-K clusters prefer to strongly bind to graphene surface with highest binding energies marked in red in Figure 6(c) (-3.137 eV for cluster-4 and -3.419 eV for cluster-5). The presence of more K atoms is one of the reasons for their strong binding with graphene.[67] Interaction strength of the other three clusters (marked in blue in Figure 6(c)) with graphene is also reasonably high upon comparison with the literature.[68] These results strongly suggest that presence of graphene substrate significantly reduces the chances of shuttle effects in K_xSe/Gr cathode. Among interfacial clusters in low K cathode, cluster-2 (Se-Se-Se centered) is more stable and interacts more strongly with graphene substrate. This binding preference is a clear suggestion of controlled polyselenide dissolution in the presence of graphene. However, as we observed an increase in binding energy with increase in Se content (Se-Se to Se-

Se-Se), discharging may not be very favorable over graphene surface in low K cathode intermediates (with increased Se_n chains).[68, 69]

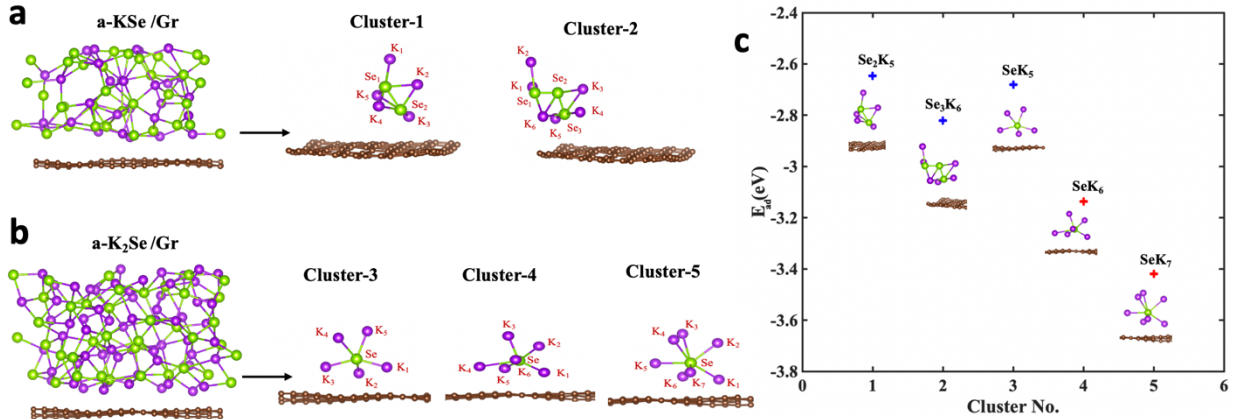


Figure 6 (a) Side view of relaxed a-KSe/Gr structure. Majority Se-Se bonds are intact, and interface contains potassium polyselenides with two to three Se atom chains at the center. These clusters are numbered as 1, 2. (b) Side view of relaxed a-K₂Se/Gr structure. Majority Se-Se bonds have broken to accommodate K and interface contains Se-K clusters with one Se atom at the center surrounded by K atoms. Clusters are numbered as 3,4 and 5. (c) Binding energies E_{ad} of different K-Se clusters noted at the interface with graphene substrate. E_{ad} of cluster 4 and 5 which are least stable in isolated state but bind strongly with graphene are marked in red.

3.3. Average Intercalation Potential.

Operation of KIB is based on rocking-chair principle of LIBs, as K ions shuttle between anode and cathode through an electrolyte. To navigate this K ion shuttling, a chemical potential difference must exist between cathode ($\mu^{cathode}$) and anode (μ^{anode}), which is referred to as open circuit voltage (OCV).

$$OCV = -\frac{\mu_K^{cathode} - \mu_K^{anode}}{zF} \quad (2)$$

Here, F is Faraday's constant, and z is the electronic charge transported by K in the electrolyte ($z = 1$ for K in non-conducting electrolyte). To theoretically calculate OCV for K_xSe cathode, K metal anode is considered with a constant chemical potential equivalent to K metal's Gibbs free energy (depicted in Figure 7(a)). Thus, electrical energy[70] gained in discharging between K_ySe and K_xSe ($x > y$) is given by difference in Gibbs free energy (G) of the two compounds as

$$E = -\left[G_{K_xSe} - G_{K_ySe} - (x - y)G_K\right] \quad (3)$$

$$E = -\Delta G \quad (4)$$

Where G_K is the total Gibbs free energy of a single K atom in metallic K unit cell, and $(x - y)$ represents K atoms intercalated in cathode during discharging. This leads us to calculate average intercalation voltage in cathode between two intercalation limits as

$$V = \frac{E}{(x-y)F} \quad (5)$$

Gibbs free energies calculated in our study are in electronvolts (eV) and are plotted for intermediate a- K_xSe/Gr structures ($0 \leq x < 2$) in Figure 7(b). Therefore F is neglected in the above equation.[71] Average voltage profiles between final discharged cathode a- K_2Se and cathode intermediates (a- K_xSe with $0 \leq x < 2$) as a function of K content are shown in Figure 7(c). A sloping voltage curve in range 1.4 – 0.38 V (pink curve in Figure 7(c)) is the result of amorphous Se forming a solid solution with K in absence of any substrate. This voltage dip upon discharging is not a characteristic of a good cathode. Furthermore, capacity of pristine Se in KIB

has been previously shown to drop to zero after first electrochemical cycle regardless of using carbonate-based electrolytes, which are best known to diminish shuttle effects caused by polyselenide formations.[25] Loss of active electrode to shuttle effects is a major drawback of using Se cathode in ion-based batteries, and high capacity potential of Se cathode can only be leveraged by combining Se with C-based matrix.[72]

In comparison with porous C, hexagonal C lattice-based matrix enclosing Se cathodes exhibit better performances for LIB.[42, 52, 53, 73] This is partially due to high conductivity of hexagonal C lattice and partly due to inability of Se to form covalent interactions with lattice surface that can cause loss of active Se electrode.[38] The blue plot in Figure 7(c) shows intercalation voltage profile of a-K_xSe cathode supported by hexagonal C lattice i.e. graphene in this case. The discharge voltage for intercalation limit $x = 0$ and $x = 2$ is 1.55 V. Two high voltage peaks are noted at $x = 0.8$ and $x = 1.6$. These peaks correspond to high energy structures ***ii*** and ***v***, as indicated in Figure 7(b). The energy of a-Se/Gr cathode dips during the discharging process except near the intermediates ***ii*** and ***v*** where the sudden energy spikes are noted. These energy spikes are possibly due to several reasons. First, the rise in energy between intermediates ***i*** and ***ii*** is due to the stability of long Se chains on the graphene surface (Se-Se-Se vs. Se-Se in Figure 6(c)) that causes an inconvenience in discharging. The increased binding energy between graphene and polyselenides with increased Se content (Se-Se to Se-Se-Se) could cause difficulty in Se chain breakage to store more K. Secondly, the two peaks in Figure 7(b) are similar to the earlier reports where electrode was recognized to constitute of two distinct phases.[74, 75] Based on this, we anticipate that these high energy structures could be caused due to irregular distribution of small Se-K ordered phases. Though we report evidence of graphene-favored Se-K clusters in the present study, we did not see any distinctive phase boundary in our nano-scale systems. Potential interface-

induced phase changes in these heterostructure electrodes could be further explored by multiscale modeling. From Figure 7(c), we can say that operating a-Se/Gr cathode at high voltage conditions ($\sim 2\text{V}$) can lead to the formation of these cathode intermediates (ii and ν) which represent thermodynamical energy barriers in the process of intercalation/deintercalation and could cause irreversible capacity losses. Moreover, parameters like K segregation at graphene interface and high binding energy of Se-K clusters (SeK_7 and SeK_6) with graphene can be factored into consideration for difficult K deintercalation in intermediate denoted as ν ($\text{K}_{1.6}\text{Se}$).

If we observe the intercalation voltage profile in Figure 7(c) upon ignoring these thermodynamical barriers (dashed red plot), the voltage remains in 1.55 - 1.38 V range and exhibits a plateau-like profile. It is possible that K undergoes a single step reaction with Se to form K_2Se near 1.55 V, much like in the case of Li-Se.[76]



This single-step reaction between chain like Se_n cathode and K has also been reported for Se encapsulated in microporous C in an experimental study by Kang and coworkers.[30] In addition to this, the voltage range for the reaction is close to cathode voltage reported in a study with Se hosted by carbon nanotube anchored microporous C.[27] Our results feature strong dependence of electrochemistry on the graphene interface present in nanostructured electrodes.

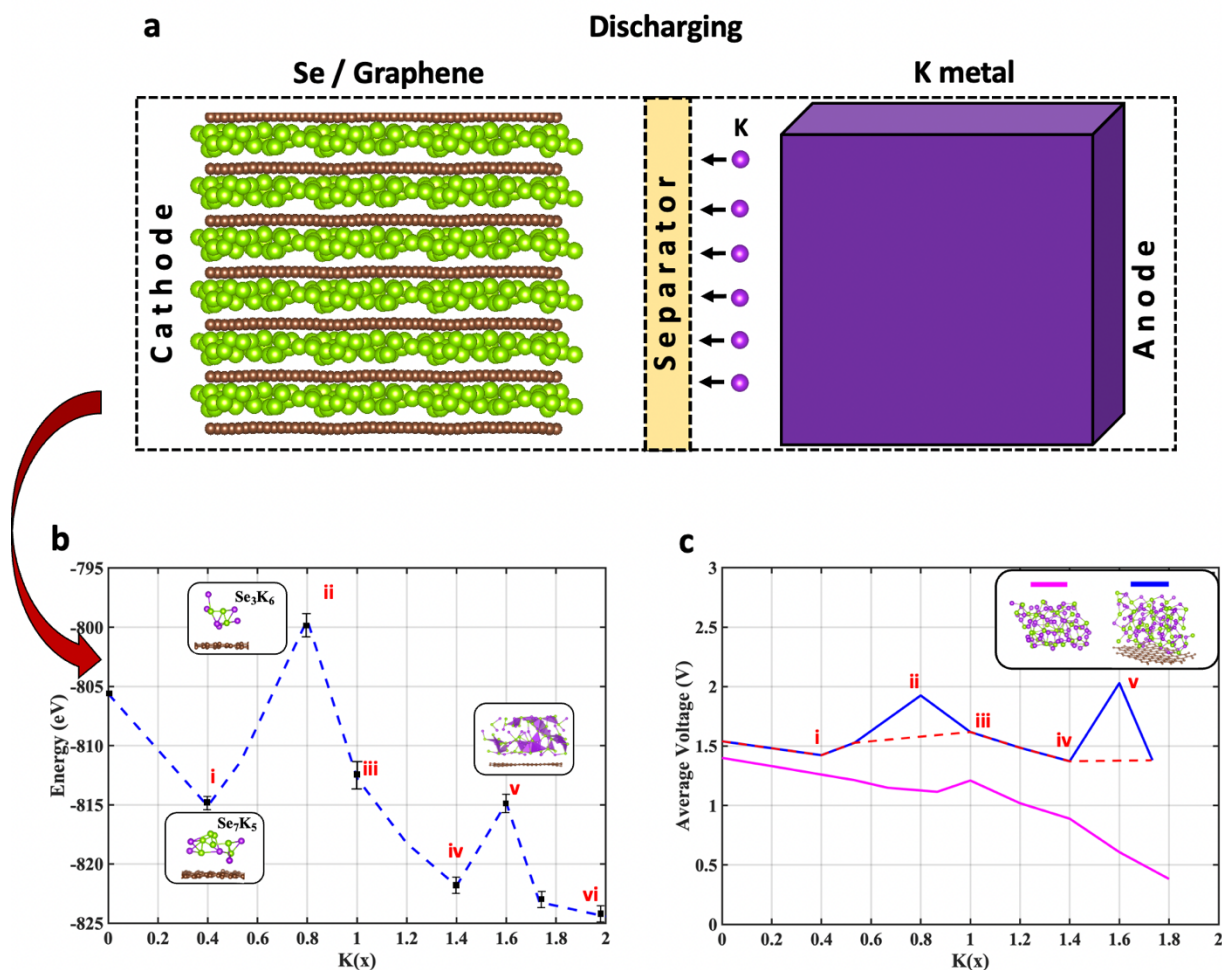


Figure 7 (a) Selenium-graphene heterostructure cathode half-cell during discharging process in KIB. (b) Energy of relaxed graphene supported $a\text{-K}_x\text{Se}$ ($0 \leq x < 2$) cathode intermediates labelled *i* to *vi*. (c) Average discharge voltage of $a\text{-K}_x\text{Se}$ cathode intermediates with K_2Se as final discharged product. The voltage profiles of Se-K alloying cathode with and without graphene substrate are plotted in blue and pink, respectively.

4. Summary

In summary, we modeled graphene-enclosed K_xSe cathode identical to experimentally designed electrodes and investigated the effect of graphene interface on K intercalation/deintercalation mechanism by AIMD and DFT. Our results suggest graphene substrate creates a substantial chemical gradient inside the K-Se cathode and induces Se-K reactivity. Increased K density near interface causes the formation of Se-K clusters with a high K atom count (SeK_6 , SeK_7). These clusters are not stable without substrate and interact strongly with graphene surface through binding energies (E_{ad}) as high as -3.137 eV for SeK_6 and -3.419 eV for SeK_7 . These strong binding preferences between clusters and graphene are needed to avoid dissolution of selenides in electrolytes. However, they can cause difficult deintercalation in several K_xSe intermediates. Moreover, the increase in binding energy with an increase in Se_n chain ($E_{ad} = -2.646$ eV for $n=2$ and $E_{ad} = -2.82$ eV for $n=3$) indicates that discharging is not favorable over graphene surface in low K cathode intermediates. These inferences appeared true when we calculated the intercalation voltage of K_xSe cathode intermediates with and without graphene support. We show that between K and Se cathode, there is a single step reaction near 1.55 V with K_2Se as discharged product. To avoid capacity losses due to difficult K intercalation/deintercalation, graphene-supported Se cathode should operate in the voltage range of 1.55V to 1.38V. High voltage can cause the formation of cathode intermediates with thermodynamically challenging K insertion and extraction.

Acknowledgements

V.S. and D.D. were supported by NSF (Award Number 1911900) during the study. D.D. acknowledges the Extreme Science and Engineering Discovery Environment (XSEDE) for the computational facilities (Award Number – DMR180013).

Competing Interest

The authors declare no competing financial interest

Data Availability

The data reported in this paper is available from the corresponding author upon reasonable request.

Code Availability

The pre- and postprocessing codes used in this paper are available from the corresponding author upon reasonable request. Restrictions apply to the availability of the simulation codes, which were used under license for this study.

Author Contributions

V.S. contributed to the work with co-conception of the project, computation, and manuscript preparation. D.D. contributed by co-conception, guidance of research, preparation of the manuscript. All authors have given approval to the final version of the manuscript.

Author Information

Vidushi Sharma is currently working as a Staff Research Scientist at IBM Almaden Research Center in San Jose, CA, USA where she joined in November, 2021 after completed her Ph.D. from New Jersey Institute of Technology (NJIT) in Mechanical Engineering.

Dibakar Datta is currently a faculty at the Department of Mechanical and Industrial Engineering, Newark College of Engineering, New Jersey Institute of Technology (NJIT), Newark, USA. He finished his Ph.D. at Brown University.

References

- [1] J.R. Dahn, T. Zheng, Y. Liu, J. Xue, Mechanisms for lithium insertion in carbonaceous materials, *Science* 270(5236) (1995) 590-593.
- [2] M.S. Whittingham, Electrical energy storage and intercalation chemistry, *Science* 192(4244) (1976) 1126-1127.
- [3] W. Zhang, Y. Liu, Z. Guo, Approaching high-performance potassium-ion batteries via advanced design strategies and engineering, *Science advances* 5(5) (2019) eaav7412.
- [4] E. De La Llave, V. Borgel, K.-J. Park, J.-Y. Hwang, Y.-K. Sun, P. Hartmann, F.-F. Chesneau, D. Aurbach, Comparison between Na-ion and Li-ion cells: understanding the critical role of the cathodes stability and the anodes pretreatment on the cells behavior, *ACS applied materials & interfaces* 8(3) (2016) 1867-1875.
- [5] V. Palomares, P. Serras, I. Villaluenga, K.B. Hueso, J. Carretero-González, T. Rojo, Na-ion batteries, recent advances and present challenges to become low cost energy storage systems, *Energy & Environmental Science* 5(3) (2012) 5884-5901.
- [6] A. Eftekhari, Potassium secondary cell based on Prussian blue cathode, *Journal of Power Sources* 126(1-2) (2004) 221-228.
- [7] S. Komaba, T. Itabashi, T. Kimura, H. Groult, N. Kumagai, Opposite influences of K⁺ versus Na⁺ ions as electrolyte additives on graphite electrode performance, *Journal of power sources* 146(1-2) (2005) 166-170.

- [8] J.C. Pramudita, D. Sehwat, D. Goonetilleke, N. Sharma, An initial review of the status of electrode materials for potassium-ion batteries, *Advanced energy materials* 7(24) (2017) 1602911.
- [9] S. Komaba, T. Hasegawa, M. Dahbi, K. Kubota, Potassium intercalation into graphite to realize high-voltage/high-power potassium-ion batteries and potassium-ion capacitors, *Electrochemistry Communications* 60 (2015) 172-175.
- [10] K. Nobuhara, H. Nakayama, M. Nose, S. Nakanishi, H. Iba, First-principles study of alkali metal-graphite intercalation compounds, *Journal of Power Sources* 243 (2013) 585-587.
- [11] M.H. Han, E. Gonzalo, G. Singh, T. Rojo, A comprehensive review of sodium layered oxides: powerful cathodes for Na-ion batteries, *Energy & Environmental Science* 8(1) (2015) 81-102.
- [12] C. Vaalma, G.A. Giffin, D. Buchholz, S. Passerini, Non-aqueous K-ion battery based on layered $K_0.3MnO_2$ and hard carbon/carbon black, *Journal of The Electrochemical Society* 163(7) (2016) A1295.
- [13] C. Zhang, Y. Xu, M. Zhou, L. Liang, H. Dong, M. Wu, Y. Yang, Y. Lei, Potassium Prussian blue nanoparticles: a low-cost cathode material for potassium-ion batteries, *Advanced Functional Materials* 27(4) (2017) 1604307.
- [14] E. Nossol, V.H. Souza, A.J. Zarbin, Carbon nanotube/Prussian blue thin films as cathodes for flexible, transparent and ITO-free potassium secondary battery, *Journal of colloid and interface science* 478 (2016) 107-116.
- [15] C.D. Wessells, S.V. Peddada, R.A. Huggins, Y. Cui, Nickel hexacyanoferrate nanoparticle electrodes for aqueous sodium and potassium ion batteries, *Nano letters* 11(12) (2011) 5421-5425.
- [16] D. Su, A. McDonagh, S.Z. Qiao, G. Wang, High-capacity aqueous potassium-ion batteries for large-scale energy storage, *Advanced Materials* 29(1) (2017) 1604007.

- [17] Q. Pang, X. Liang, C.Y. Kwok, L.F. Nazar, Advances in lithium–sulfur batteries based on multifunctional cathodes and electrolytes, *Nature Energy* 1(9) (2016) 1-11.
- [18] G. Xu, B. Ding, J. Pan, P. Nie, L. Shen, X. Zhang, High performance lithium–sulfur batteries: advances and challenges, *Journal of Materials Chemistry A* 2(32) (2014) 12662-12676.
- [19] D. Su, D. Zhou, C. Wang, G. Wang, Lithium-Sulfur Batteries: Toward High Performance Lithium–Sulfur Batteries Based on Li₂S Cathodes and Beyond: Status, Challenges, and Perspectives (*Adv. Funct. Mater.* 38/2018), *Advanced Functional Materials* 28(38) (2018) 1870273.
- [20] L. Liu, Y. Hou, X. Wu, S. Xiao, Z. Chang, Y. Yang, Y. Wu, Nanoporous selenium as a cathode material for rechargeable lithium–selenium batteries, *Chemical communications* 49(98) (2013) 11515-11517.
- [21] J.T. Lee, H. Kim, M. Oschatz, D.C. Lee, F. Wu, H.T. Lin, B. Zdyrko, W.I. Cho, S. Kaskel, G. Yushin, Micro-and Mesoporous Carbide-Derived Carbon–Selenium Cathodes for High-Performance Lithium Selenium Batteries, *Advanced energy materials* 5(1) (2015) 1400981.
- [22] Y. Cui, A. Abouimrane, J. Lu, T. Bolin, Y. Ren, W. Weng, C. Sun, V.A. Maroni, S.M. Heald, K. Amine, (De) Lithiation mechanism of Li/SeS_x ($x= 0-7$) batteries determined by in situ synchrotron X-ray diffraction and X-ray absorption spectroscopy, *Journal of the American chemical society* 135(21) (2013) 8047-8056.
- [23] C.P. Yang, S. Xin, Y.X. Yin, H. Ye, J. Zhang, Y.G. Guo, An advanced selenium–carbon cathode for rechargeable lithium–selenium batteries, *Angewandte Chemie International Edition* 52(32) (2013) 8363-8367.

- [24] H. Liu, Q. Wang, X. Sun, H. Gou, C. Zhang, G. Wang, Carbon host pore structure regulation boosting fast and stable Se-K electrochemistry towards Se-K ion capacitors, *Carbon* 203 (2023) 141-151.
- [25] Y. Liu, Z. Tai, Q. Zhang, H. Wang, W.K. Pang, H.K. Liu, K. Konstantinov, Z. Guo, A new energy storage system: Rechargeable potassium-selenium battery, *Nano Energy* 35 (2017) 36-43.
- [26] T. Yang, Y. Niu, Q. Liu, M. Xu, Cathode host engineering for non-lithium (Na, K and Mg) sulfur/selenium batteries: A state-of-the-art review, *Nano Materials Science* (2022).
- [27] X. Zhou, L. Wang, Y. Yao, Y. Jiang, R. Xu, H. Wang, X. Wu, Y. Yu, Integrating Conductivity, Captivity, and Immobility Ability into N/O Dual-Doped Porous Carbon Nanocage Anchored with CNT as an Effective Se Host for Advanced K-Se Battery, *Advanced Functional Materials* 30(43) (2020) 2003871.
- [28] X. Huang, W. Wang, J. Deng, W. Gao, D. Liu, Q. Ma, M. Xu, A Se-hollow porous carbon composite for high-performance rechargeable K–Se batteries, *Inorganic Chemistry Frontiers* 6(8) (2019) 2118-2125.
- [29] X. Huang, J. Deng, Y. Qi, D. Liu, Y. Wu, W. Gao, W. Zhong, F. Zhang, S. Bao, M. Xu, A highly-effective nitrogen-doped porous carbon sponge electrode for advanced K–Se batteries, *Inorganic Chemistry Frontiers* 7(5) (2020) 1182-1189.
- [30] J.K. Kim, Y.C. Kang, Encapsulation of Se into Hierarchically Porous Carbon Microspheres with Optimized Pore Structure for Advanced Na–Se and K–Se Batteries, *ACS nano* 14(10) (2020) 13203-13216.
- [31] D. Li, L. Wang, X. Cheng, Y. Yao, Y. Jiang, P. Shi, Y. Wu, X. Wu, C. Ma, Y. Yu, Manipulating selenium molecular configuration in N/O dual-doped porous carbon for high performance potassium-ion storage, *Journal of Energy Chemistry* 62 (2021) 581-589.

- [32] R. Xu, Y. Yao, H. Wang, Y. Yuan, J. Wang, H. Yang, Y. Jiang, P. Shi, X. Wu, Z. Peng, Unraveling the Nature of Excellent Potassium Storage in Small-Molecule Se@ Peapod-Like N-Doped Carbon Nanofibers, *Advanced materials* 32(52) (2020) 2003879.
- [33] A. Abouimrane, D. Dambournet, K.W. Chapman, P.J. Chupas, W. Weng, K. Amine, A new class of lithium and sodium rechargeable batteries based on selenium and selenium–sulfur as a positive electrode, *Journal of the American chemical society* 134(10) (2012) 4505-4508.
- [34] C.P. Yang, S. Xin, Y.X. Yin, H. Ye, J. Zhang, Y.G. Guo, An advanced selenium–carbon cathode for rechargeable lithium–selenium batteries, *Angewandte Chemie* 125(32) (2013) 8521-8525.
- [35] P. Xue, Y. Zhai, N. Wang, Y. Zhang, Z. Lu, Y. Liu, Z. Bai, B. Han, G. Zou, S. Dou, Selenium@ Hollow mesoporous carbon composites for high-rate and long-cycling lithium/sodium-ion batteries, *Chemical Engineering Journal* 392 (2020) 123676.
- [36] J. Ding, H. Zhou, H. Zhang, L. Tong, D. Mitlin, Selenium impregnated monolithic carbons as free-standing cathodes for high volumetric energy lithium and sodium metal batteries, *Advanced Energy Materials* 8(8) (2018) 1701918.
- [37] S. Basu, S. Suresh, K. Ghatak, S.F. Bartolucci, T. Gupta, P. Hundekar, R. Kumar, T.-M. Lu, D. Datta, Y. Shi, Utilizing van der Waals slippery interfaces to enhance the electrochemical stability of silicon film anodes in lithium-ion batteries, *ACS applied materials & interfaces* 10(16) (2018) 13442-13451.
- [38] V. Sharma, D. Mitlin, D. Datta, Understanding the Strength of the Selenium–Graphene Interfaces for Energy Storage Systems, *Langmuir* 37(6) (2021) 2029-2039.

- [39] R. Cai, X. Chen, P. Liu, T. Chen, W. Liu, X. Fan, B. Ouyang, K. Liu, A Novel Cathode Based on Selenium Confined in Biomass Carbon and Graphene Oxide for Potassium-Selenium Battery, *ChemElectroChem* 7(21) (2020) 4477-4483.
- [40] Z. Li, L. Yuan, Z. Yi, Y. Liu, Y. Huang, Confined selenium within porous carbon nanospheres as cathode for advanced Li–Se batteries, *Nano Energy* 9 (2014) 229-236.
- [41] K. Xi, P.R. Kidambi, R. Chen, C. Gao, X. Peng, C. Ducati, S. Hofmann, R.V. Kumar, Binder free three-dimensional sulphur/few-layer graphene foam cathode with enhanced high-rate capability for rechargeable lithium sulphur batteries, *Nanoscale* 6(11) (2014) 5746-5753.
- [42] J. Zhang, Y. Xu, L. Fan, Y. Zhu, J. Liang, Y. Qian, Graphene–encapsulated selenium/polyaniline core–shell nanowires with enhanced electrochemical performance for Li–Se batteries, *Nano Energy* 13 (2015) 592-600.
- [43] D. Kundu, F. Krumeich, R. Nesper, Investigation of nano-fibrous selenium and its polypyrrole and graphene composite as cathode material for rechargeable Li-batteries, *Journal of power sources* 236 (2013) 112-117.
- [44] N. Deng, Y. Feng, G. Wang, X. Wang, L. Wang, Q. Li, L. Zhang, W. Kang, B. Cheng, Y. Liu, Rational structure designs of 2D materials and their applications toward advanced lithium-sulfur battery and lithium-selenium battery, *Chemical Engineering Journal* 401 (2020) 125976.
- [45] J. Ding, H. Zhou, H. Zhang, T. Stephenson, Z. Li, D. Karpuzov, D. Mitlin, Exceptional energy and new insight with a sodium–selenium battery based on a carbon nanosheet cathode and a pseudographite anode, *Energy & Environmental Science* 10(1) (2017) 153-165.
- [46] K. Han, Z. Liu, H. Ye, F. Dai, Flexible self-standing graphene–Se@ CNT composite film as a binder-free cathode for rechargeable Li–Se batteries, *Journal of Power Sources* 263 (2014) 85-89.

- [47] D. Huang, S. Li, Y. Luo, X. Xiao, L. Gao, M. Wang, Y. Shen, Graphene oxide-protected three dimensional Se as a binder-free cathode for Li-Se battery, *Electrochimica Acta* 190 (2016) 258-263.
- [48] C. Luo, Y. Xu, Y. Zhu, Y. Liu, S. Zheng, Y. Liu, A. Langrock, C. Wang, Selenium@mesoporous carbon composite with superior lithium and sodium storage capacity, *ACS nano* 7(9) (2013) 8003-8010.
- [49] C. Escoffery, S. Halperin, Studies on the Polymorphic Transformation of Selenium, *Transactions of The Electrochemical Society* 90(1) (1946) 163.
- [50] A. Goldan, C. Li, S. Pennycook, J. Schneider, A. Blom, W. Zhao, Molecular structure of vapor-deposited amorphous selenium, *Journal of Applied Physics* 120(13) (2016) 135101.
- [51] X. Peng, L. Wang, X. Zhang, B. Gao, J. Fu, S. Xiao, K. Huo, P.K. Chu, Reduced graphene oxide encapsulated selenium nanoparticles for high-power lithium–selenium battery cathode, *Journal of Power Sources* 288 (2015) 214-220.
- [52] K. Han, Z. Liu, J. Shen, Y. Lin, F. Dai, H. Ye, A free-standing and ultralong-life lithium-selenium battery cathode enabled by 3D mesoporous carbon/graphene hierarchical architecture, *Advanced functional materials* 25(3) (2015) 455-463.
- [53] L. Sha, P. Gao, X. Ren, Q. Chi, Y. Chen, P. Yang, A Self-Repairing Cathode Material for Lithium–Selenium Batteries: Se–C Chemically Bonded Selenium–Graphene Composite, *Chemistry–A European Journal* 24(9) (2018) 2151-2156.
- [54] G.-L. Xu, T. Ma, C.-J. Sun, C. Luo, L. Cheng, Y. Ren, S.M. Heald, C. Wang, L. Curtiss, J. Wen, Insight into the capacity fading mechanism of amorphous Se₂S₅ confined in micro/mesoporous carbon matrix in ether-based electrolytes, *Nano letters* 16(4) (2016) 2663-2673.

- [55] G. Kresse, J. Furthmüller, Efficient iterative schemes for ab initio total-energy calculations using a plane-wave basis set, *Physical review B* 54(16) (1996) 11169.
- [56] G. Kresse, D. Joubert, From ultrasoft pseudopotentials to the projector augmented-wave method, *Physical Review B* 59(3) (1999) 1758.
- [57] P.E. Blöchl, Projector augmented-wave method, *Physical review B* 50(24) (1994) 17953.
- [58] J.P. Perdew, K. Burke, M. Ernzerhof, Generalized gradient approximation made simple, *Physical review letters* 77(18) (1996) 3865.
- [59] M. Dion, H. Rydberg, E. Schröder, D.C. Langreth, B.I. Lundqvist, Van der Waals density functional for general geometries, *Physical review letters* 92(24) (2004) 246401.
- [60] J. Klimeš, D.R. Bowler, A. Michaelides, Chemical accuracy for the van der Waals density functional, *Journal of Physics: Condensed Matter* 22(2) (2009) 022201.
- [61] J. Klimeš, D.R. Bowler, A. Michaelides, Van der Waals density functionals applied to solids, *Physical Review B* 83(19) (2011) 195131.
- [62] C. Liu, Z.G. Neale, G. Cao, Understanding electrochemical potentials of cathode materials in rechargeable batteries, *Materials Today* 19(2) (2016) 109-123.
- [63] G. Ceder, K. Persson, *The materials project: A materials genome approach*, 2010.
- [64] P. Xue, Y. Zhai, N. Wang, Y. Zhang, Z. Lu, Y. Liu, Z. Bai, B. Han, G. Zou, S. Dou, Selenium@ Hollow mesoporous carbon composites for high-rate and long-cycling lithium/sodium-ion batteries, *Chemical Engineering Journal* (2019) 123676.
- [65] Z. Zhang, X. Yang, Z. Guo, Y. Qu, J. Li, Y. Lai, Selenium/carbon-rich core-shell composites as cathode materials for rechargeable lithium-selenium batteries, *Journal of Power Sources* 279 (2015) 88-93.

- [66] J. Zhou, M. Chen, T. Wang, S. Li, Q. Zhang, M. Zhang, H. Xu, J. Liu, J. Liang, J. Zhu, Covalent Selenium Embedded in Hierarchical Carbon Nanofibers for Ultra-High Areal Capacity Li-Se Batteries, *Iscience* 23(3) (2020) 100919.
- [67] K. Nakada, A. Ishii, First-principles investigation of charge density analysis of various adatom adsorptions on graphene, *AIP Conference Proceedings*, American Institute of Physics, 2011, pp. 793-794.
- [68] G.-L. Xu, J. Liu, R. Amine, Z. Chen, K. Amine, Selenium and selenium–sulfur chemistry for rechargeable lithium batteries: interplay of cathode structures, electrolytes, and interfaces, *ACS energy letters* 2(3) (2017) 605-614.
- [69] S. Mukherjee, L. Kavalsky, K. Chattopadhyay, C.V. Singh, Adsorption and diffusion of lithium polysulfides over blue phosphorene for Li–S batteries, *Nanoscale* 10(45) (2018) 21335-21352.
- [70] M. Aydinol, A. Kohan, G. Ceder, K. Cho, J. Joannopoulos, Ab initio study of lithium intercalation in metal oxides and metal dichalcogenides, *Physical Review B* 56(3) (1997) 1354.
- [71] K. Ghatak, S. Basu, T. Das, V. Sharma, H. Kumar, D. Datta, Effect of cobalt content on the electrochemical properties and structural stability of NCA type cathode materials, *Physical Chemistry Chemical Physics* 20(35) (2018) 22805-22817.
- [72] A. Eftekhari, The rise of lithium–selenium batteries, *Sustainable energy & fuels* 1(1) (2017) 14-29.
- [73] X. Wang, Z. Zhang, Y. Qu, G. Wang, Y. Lai, J. Li, Solution-based synthesis of multi-walled carbon nanotube/selenium composites for high performance lithium–selenium battery, *Journal of Power Sources* 287 (2015) 247-252.

[74] M. Wagemaker, F.M. Mulder, A. Van der Ven, The role of surface and interface energy on phase stability of nanosized insertion compounds, *Advanced Materials* 21(25-26) (2009) 2703-2709.

[75] A. Van der Ven, K. Garikipati, S. Kim, M. Wagemaker, The role of coherency strains on phase stability in Li_xFePO_4 : needle crystallites minimize coherency strain and overpotential, *Journal of the Electrochemical Society* 156(11) (2009) A949.

[76] Q. Li, H. Liu, Z. Yao, J. Cheng, T. Li, Y. Li, C. Wolverton, J. Wu, V.P. Dravid, Electrochemistry of selenium with sodium and lithium: Kinetics and reaction mechanism, *ACS nano* 10(9) (2016) 8788-8795.